Band mapping in x-ray photoelectron spectroscopy: An experimental and theoretical study of W(110) with 1.25 keV excitation

C. Papp,[1,2] L. Plucinski,[3,*] J. Minar,[4] J. Braun,[4] H. Ebert,[4] C. M. Schneider,[3] and C. S. Fadley[1,2]

[1]*Materials Science Division, Lawrence Berkeley National Laboratory, One Cyclotron Road, Berkeley, California 94720, USA*
[2]*Department of Physics, University of California Davis, One Shields Road, Davis, California 95616, USA*
[3]*Peter Grünberg Institut PGI-6, Forschungszentrum Jülich, D-52425 Jülich, Germany*
[4]*Ludwig-Maximilians-Universität, München, Department Chemie und Biochemie, Physikalische Chemie, Butenandtstraße 11, D-81377 München, Germany*

Angle-resolved photoemission spectroscopy (ARPES) has generally been carried out at energies below ~150 eV, but there is growing interest in going to higher energies so as to achieve greater bulk sensitivity. To this end, we have measured ARPES spectra from a tungsten (110) crystal in a plane containing the [100], [110], and [010] directions with a photon energy of 1253.6 eV. The experimental data are compared to free-electron final-state calculations in an extended zone scheme with no inclusion of matrix elements, as well as highly accurate one-step theory including matrix elements. Both models provide further insight into such future higher-energy ARPES measurements. Special effects occurring in a higher-energy ARPES experiment, such as photon momentum, phonon-induced zone averaging effects, and the degree of cryogenic cooling required are discussed, together with qualitative predictions via appropriate Debye-Waller factors for future experiments with a number of representative elements being presented.

PACS number(s): 79.60.−i, 71.20.−b

I. INTRODUCTION

The properties of novel materials like superconductivity, metal-to-insulator transitions, heavy-fermion behavior, and half-metallic ferromagnetism are of great interest and are crucially linked to their electronic structure. Angle-resolved photoemission spectroscopy (ARPES) has developed over the past several decades into the technique of choice for determining the electronic structure of any new material, and it is thus, in some respects, a very mature tool in materials physics.[1,2] Investigators have always realized, however, that the results obtained are restricted in sensitivity to the near surface of the systems studied, due to the short inelastic mean free paths (IMFPs) of the low energy electrons used, which normally do not exceed ~150 eV in kinetic energy.[3] Thus, the bulk properties of principal interest in many materials may not always be accessible, as discussed elsewhere.[4–7]

To overcome this limitation of surface sensitivity, one can think of using higher-energy x rays in the keV or even multi-keV regime to access deeper-lying layers in a sample, thus sampling more truly bulk properties. A limited number of studies has been made to date up to ~800 eV.[8–11]

Going higher in energy nevertheless comes with some additional challenges for the interpretation of the data obtained. Obviously, a very high-energy resolution is more difficult to achieve in the keV regime, and this is complicated by the potential effects of energy shifts and smearing due to recoil.[12,13] In addition, deviations from the dipole approximation in photoelectron excitation mean that the momentum of the photon, which is negligible in the case of low energy photons, can result in a nonnegligible shift of the position of the initial-state wave vector in the reduced Brillouin zone (BZ), as pointed out some time ago.[10,14,15] Phonon creation and annihilation during photoemission also smear out the specification of the initial state in the BZ via wave-vector ($\vec{k}$) conservation, and lead to the need for cryogenic cooling

to minimize such phonon effects in order to more clearly observe direct or $\vec{k}$ conserving transitions, with such effects expected to vary with the degree of localization.[16–21] As a semiquantitative predictor of the effects of phonons, the total intensity $I_{\mathrm{Tot}}(E,\vec{k})$ at a given energy E and $\vec{k}$ can be roughly divided into zero-phonon direct transitions $I_{\mathrm{DT}}(E,\vec{k})$ and phonon-assisted nondirect transitions $I_{\mathrm{NDT}}(E,\vec{k})$ as:

$$I_{\mathrm{Tot}}(E,\vec{k}) = \mathrm{W}(T)I_{\mathrm{DT}}(E,\vec{k}) + [1 - W(T)I_{\mathrm{NDT}}(E,\vec{k})], \quad (1)$$

where $W(T)$ is the relevant photoemission Debye-Waller factor, and can be calculated from $W(T)=\exp[-\frac{1}{3}\mathrm{g}_{hk\ell}^2\langle U^2(T)\rangle]$, where g_{hkl} is the magnitude of the bulk reciprocal lattice vector involved in the direct transitions at a given photon energy and $\langle U^2(\mathrm{T})\rangle$ is the three-dimensional mean-squared vibrational displacement.

Accessing more bulklike electronic properties of materials thus poses new challenges for the instrumentation used. The significantly lower valence-level photoelectric cross sections and the considerably larger linewidths of most harder x-ray sources pose problems of intensity and resolution, although by now high-resolution, high-flux, hard x-ray beamlines at third generation synchrotron sources are available, and these are further advancing this field. Also, the combined analyzer resolution in terms of energy and angle have to be considered, as higher-energy ARPES data will span a considerably smaller angular width in traversing a BZ than is the case for measurements at much lower energies. Nonetheless, these challenges have not prevented researchers from obtaining ARPES data at up to ~800 eV with current energy-and-angle-resolving hemispherical analyzers,[8–11,22–24] thus marking significant steps forward compared to the first studies.[14,15] In this paper, we consider using x rays with 1253.6 eV from a laboratory Mg Kα source as an important reference for such measurements. The datasets have been obtained over a more extended angle range than in prior work, and we also consider in more detail

the $\vec{k}$ dependence of phonon effects. All of the issues dealt with here are thus relevant to future studies with even higher-energy x rays in the multi-keV regime.

In this study, we present angle-resolved photoemission data from tungsten (110) taken with a standard nonmonochromatized Mg Kα laboratory source, as a convenient demonstration study that permits understanding on a basic level the effects that are to be considered when using harder x rays to study more bulklike electronic properties. At this photon energy, it is often thought that one has reached the so-called x-ray photoemission spectroscopy (XPS) limit, with $W(T) \approx 0$, and valence-band spectra thus representing a matrix-element-weighted densities of states (DOS) instead of what is found in the ultraviolet photoemission spectroscopy (UPS) or ARPES limit: $\vec{k}$-resolved matrix-element-weighted band-structure results. Tungsten (110) was chosen as a model system that has been well studied, from both experimental[4,14,15,25,26] as well as theoretical[16,27,28] points of view. But a principal reason for choosing it here is its excellent properties for high-energy ARPES. First, tungsten has a broad valence-band distribution in energy and strongly dispersing bands, thus somewhat relaxing the requirements on both energy and angle resolution. Second, it has been known for some time that it is among the few best elements as far as suppressing phonon effects in ARPES;[14,15] this is due to its high Debye temperature and its high atomic mass, which overall permits observing a high degree of direct-transition behavior at higher photon energies. For tungsten at an excitation energy of 1253.6 eV, this yields $W(T) = 0.82$ at 77 K and 0.60 at 300 K, the two temperatures studied here.

The resulting data were analyzed via two models: a simple free-electron final-state $\vec{k}$-conserving calculation in an extended-zone scheme that neglects matrix-element effects, and a much more rigorous one-step theory based on the layer–Korringa-Kohn-Rostoker (KKR) method which includes matrix elements and the presence of the surface (for more details on this see Refs. 17 and 29). Both methods provide insight into the fundamental physics of the experiment and lead to further conclusions as to the possibilities for hard x-ray angle-resolved photoelectron spectroscopy on other materials.

II. EXPERIMENTAL

The data were taken with the Multi-Technique Spectrometer/Diffractometer at the Lawrence Berkeley National Laboratory (for more details see Ref. 30). The system is equipped with a Scienta SES200 spectrometer upgraded to SES2002 performance that is oriented at the "magic angle" of 54.7° relative to a dual-anode x-ray source, here used to generate 1253.6-eV Mg Kα x rays at 300 W power. The real-space experimental geometry is shown in Fig. 1, together with the relevant momentum conservation relations involving the final photoelectron wave vector $\vec{k}_f$ in an extended-zone scheme and calculated inside the crystal and adjusted for the inner potential, the initial-state wave vector $\vec{k}_i$ in the reduced BZ, a possible surface reciprocal lattice vector $\vec{g}_{surf}$ that will become negligible as energy is increased, and a phonon wave vector $\vec{q}_{phonon}$ that will act to smear out the determination of $\vec{k}_i$. In this magic-angle configuration, differential photoelectric

$$\vec{k}_f = \vec{k}_i + \vec{g}_{hk\ell} + \vec{k}_{h\nu} + \vec{g}_{surf} + \vec{q}_{phonon}$$

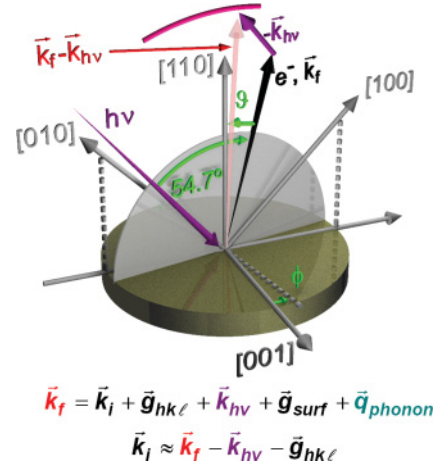$$\vec{k}_i \approx \vec{k}_f - \vec{k}_{h\nu} - \vec{g}_{hk\ell}$$

FIG. 1. (Color online) The real-space geometry of the experiment, with the key wave-vector conservation rules indicated.

cross sections in the dipole approximation are proportional to the total cross section. The spectrometer was operated in angle-resolving mode, with each two-dimensional energy-vs-angle detector image spanning ∼18°. By means of sample rotation in the angle θ with steps of ∼10°, several detector images with all directions lying very close to the plane defined by the [010], [110] = surface normal, and [100] directions. The emission direction was varied from ∼–12° to +46° relative to [110], as shown in Fig. 1. One type of misalignment of the sample is shown by the azimuthal rotation angle ϕ in Fig. 1, and we consider the effect of another type of tilt misalignment later.

Angular resolution is of course important in our measurements, and the lens system in our upgraded SES2002 has been estimated from electron-optical calculations to provide a resolution of below 0.5° for an x-ray beam spot of 3 mm diam. Although the effective beam spot with a nonmonochromatized x-ray tube as in our current experiments was much larger, measuring core-level intensities showed that only tungsten core levels were present in the spectra, even though the sample was mounted on a Mo holder. This behavior must result from the electron-optical properties of the SES2002 electrostatic lens system, which, even in angular mode, limits the effective field of view. Also, measuring W 4f photoelectron diffraction, and the various sharp features within it, permitted estimating the angular resolution experimentally. Overall, our results indicate that the angular resolution in the present study was below 1°. In future experiments with a monochromatized and collimated laboratory x-ray source or a highly focused synchrotron radiation beam it should be possible to improve this to ∼0.1°.

The 10-mm-diam tungsten sample was cleaned by standard procedures of oxygen exposure and flashing to 2500 K. The sample cleanliness was checked with core-level XPS.

III. RESULTS

In Fig. 2(a), we summarize the raw data from our ARPES measurements taken with the Mg Kα source over a range of ∼50° at room temperature. Figure 2(b) then shows the same set of measurements at liquid nitrogen temperature. One can see that cooling the sample results in sharper features in several
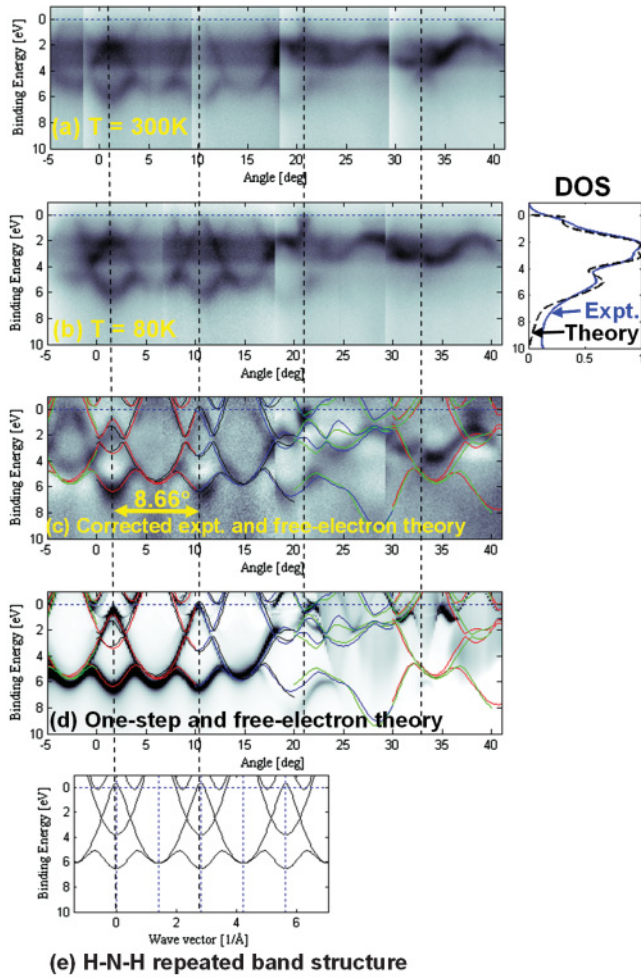
FIG. 2. (Color online) (a) The raw experimental data, taken at room temperature, with no correction for the weak nondispersing density-of-states-like background. (b) The raw experimental data, taken at liquid nitrogen temperature. At right here, we also show the angle-integrated intensity, in comparison to a simple DOS from GGA theory. (c) Experimental data that have been corrected for phonon effects and photoelectron diffraction using the two-step normalization in Eqs. (2)–(5). Overlaid on this are curves representing simple free-electron final-state theory. (d) The results of one-step photoemission calculations, including matrix-element effects, with free-electron final-state theory curves again overlaid. (e) The repeated band structure of tungsten along H-N-H, which Fig. 3(c) indicates should be approximately sampled in the angle region covered by reciprocal lattice vectors $\vec{g}_1$ and $\vec{g}_2$.

places, due to the reduced phonon broadening. At the right in Fig. 2(b), we also show the angle-integrated version of the low-temperature data, in comparison to the density of states as calculated by the Wien2k linearized augmented-plane-wave (LAPW) all-electron program, using the generalized gradient approximation (GGA) exchange-correlation functional.[31] Not surprisingly, this extensive angle integration, which in turn corresponds to integrating over various regions in the BZ (see further discussion and figures in this section) leads to a high degree of agreement between experiment and a theoretical DOS, directly corresponding to the XPS limit. Each of the wide range angular maps shown in Figs. 2(a) and 2(b) took ∼12 h to measure, at an x-ray tube power of only 300 W.

In Fig. 2(c), we also show the results of applying one promising method due to Bostwick and Rotenberg[32] of correcting the raw experimental data for the effects of density-of-states-like intensity due to phonon excitations, via a quantity noted $N'(E)$, as well as x-ray photoelectron diffraction, via a quantity noted $N(\theta)$. In this method, a two-step normalization of each detector image $I_{\text{expt}}(E,\theta)$ is carried out in both kinetic energy E and emission angle θ, as follows:

$$N(\theta) = \int I_{\text{expt}}(E,\theta)\,dE, \qquad (2)$$

$$I(E,\theta) = I_{\text{expt}}(E,\theta)/N(\theta), \qquad (3)$$

$$N'(E) = \int I(E,\theta)\,d\theta, \qquad (4)$$

$$I'(E,\theta) = I(E,\theta)/N'(E). \qquad (5)$$

It is then $I'(E,\theta)$ that is plotted in Fig. 2(c). In the XPS limit of high energy and/or temperature, $N(\theta)$ will converge to an angular distribution controlled by photoelectron diffraction effects,[21] and $N'(E)$ should converge to a matrix-element-weighted density of states. From the point of view of ARPES, this normalization will tend to obscure matrix-element effects somewhat, as $N(\theta)$ at lower energies and/or temperatures will contain modulations associated with the BZ periodicity [cf. Fig. 2(b)], and division by $N'(E)$ will tend to enhance weaker features. However, this normalization has the advantage of enhancing all features due to band dispersions, and reducing those due to DOS-like or x-ray photoelectron diffraction (XPD)-like intensity. This benefit is obvious in comparing Figs. 2(b) and 2(c).

The corrected results from Fig. 2(c) are also compared in an overlay with theoretical calculations based on a simple free-electron (FE) model and $\vec{k}$ conservation via the simplest picture of $\vec{k}_i = \vec{k}_f - \vec{k}_{h\nu} - \vec{g}_{hk\ell}$. It is clear that the FE model, which incorporates a band structure $E_i(\vec{k}_i)$ calculated using local density theory, yields an excellent description of the positions of many features over the full range of the data, particularly over the angle range of $\theta \sim -2°$ to 30° as measured relative to the [110] surface normal. The FE curves are calculated for each orientation of the sample and shown in different colors. These curves span an angle range that permits us, via their overlap, to notice the slight differences of ∼1°–2° in calculated peak positions due to the discrete changes made in the photon momentum. Thus, the panels in Fig. 2(b) are not, strictly speaking, a continuous juxtaposition in angle of the ARPES data. The dashed vertical lines in Fig. 2 indicate correspondence between a number of features in experiment and theory.

In Fig. 2(d), we now show the results of one-step model calculations,[29,33] and these are again compared to the simple free-electron final-state curves. The two very different theoretical approaches are in remarkably good agreement as to many features, particularly over the angle range of ∼−5° to +25°, but even beyond that. Comparing experiment in Fig. 2(c) and one-step theory in Fig. 2(d), we also note excellent agreement as to the positions and relative intensities of many features. Deviations are seen between theory and experiment above an angle of ∼30°, but these may be due to a small sample tilt relative to the ideal geometry, as discussed further in

this section. It should also be noted that these calculations continuously vary the direction of the photon wave vector as the sample is rotated to span the angle range. Thus, they do not exactly simulate the detector panels in experiment, with some aspects of this also being discussed in connection with the FE calculations, which do hold the photon wave vector fixed over a single detector image. As a final point concerning the one-step calculations, although the inclusion of photon wave vector implies a breakdown of the dipole approximation, it is nonetheless found that the inclusion of quadrupolar matrix elements is not significant in the final results. The essential point is that the shift of $\vec{k}_i = \vec{k}_f - \vec{k}_{h\nu} - \vec{g}_{hk\ell}$ due to the $\vec{k}_{h\nu}$ correction leads to larger changes in the predicted ARPES spectra than those associated with additionally including quadrupole matrix elements.

To provide further insight into these results, Fig. 3 shows the geometry in $\vec{k}$ space, including in (a) the nature of the emission direction scan, in (b) the correction due to photon wave vector, and in (c) an extended-zone view in the [100]-[110]-[010] plane of the various reciprocal lattice vectors involved in a free-electron model as direction is scanned.

The sector of the circle shown in red in Fig. 3(c) corresponds to the arc traversed by $\vec{k}_f - \vec{k}_{h\nu}$, which has a magnitude of $9.35\frac{2\pi}{a}$ [cf. Fig. 3(b)]; also indicated are the various g vectors involved in most of our data. For $[\vec{k}_f - \vec{k}_{h\nu}]$ along the [110] direction, the g vector involved is indicated as $\vec{g}_1$ and its length is $6 \times 1.414\frac{2\pi}{a} = 8.48\frac{2\pi}{a}$. Subtracting this from $|\vec{k}_f - \vec{k}_{h\nu}|$ yields $0.866\frac{2\pi}{a}$, which is very close to the Γ-N distance in the first BZ of $0.707\frac{2\pi}{a}$ (actually just outside the first BZ, but close enough for this discussion). Thus, we expect to sample states very near N for this direction. Furthermore, the large diameter of $|\vec{k}_f - \vec{k}_{h\nu}|$ means that scanning angle near normal should essentially move the sample point along a nearly straight line, thus sampling repeated H-N-H regions, as given in the repeated band-structure diagram based on the results of Wien2k GGA calculations we have performed, as shown in Fig. 2(e). This repeated pattern is in fact seen in experiment, in the free-electron final-state calculations, and in the one-step calculations over an ~20° range (from –4° to +16° in emission angle). For emission angles larger than this, additional g vectors and regions of the first BZ come into play, as expected from Fig. 3(c) and observed in Figs. 2(b) and 2(c). The resemblance of the data to the FE model in Fig. 2 is remarkable, and these results thus indicate a significant advantage of interpretation in higher-energy ARPES.

It is also noteworthy that the angular acceptance of a detector image in the analyzer (~18°) allows recording several traversals through the BZ. Initially these pass very nearly through a few H-N-H regions, as mentioned previously. However, for higher angles, corresponding to g vectors $\vec{g}_3$, $\vec{g}_4$, and $\vec{g}_5$, the curve traced out in the BZ moves away from the N-H-N line, finally being expected with $\vec{g}_3$ and $\vec{g}_4$ to roughly traverse H-Γ-H, along a direction not normally calculated in band structures.

The mating of angle scales between theory and experiment in Fig. 2 is also worth comment. The theoretical H-N-H distance in angle based on the scanning of $\vec{k}_f - \vec{k}_{h\nu}$ along
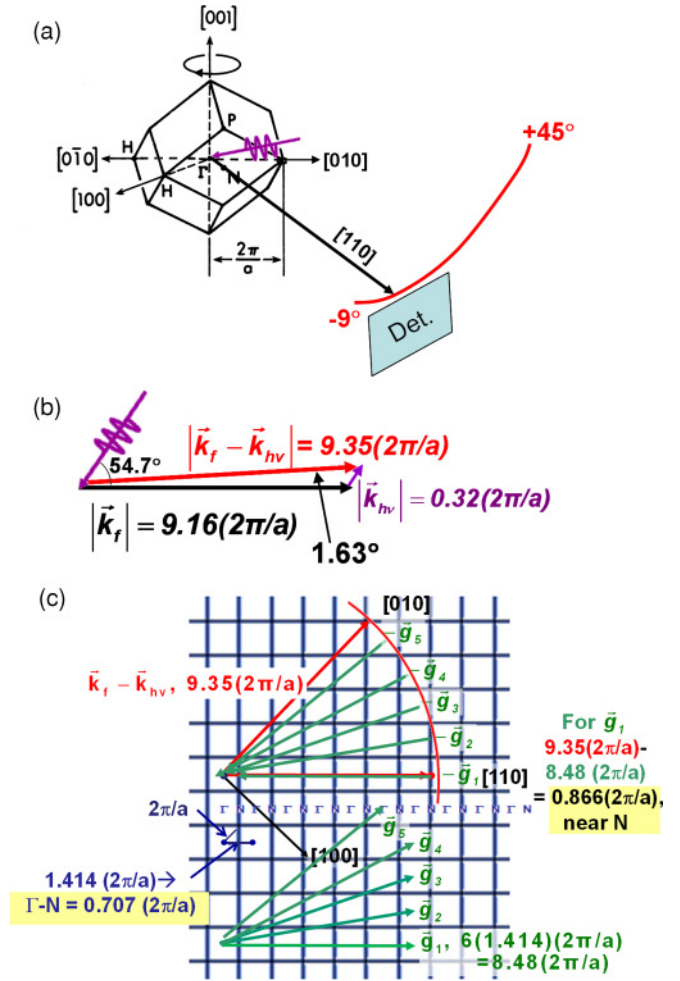

FIG. 3. (Color online) The reciprocal-space geometry of the experiment. (a) The tungsten Brillouin zone, with the range of directions spanned by our detector images indicated by the red arc. (b) The correction for photon momentum, indicating a 1.63° shift of $\vec{k}_f - \vec{k}_{h\nu}$ relative to the actual emission direction. (c) The reciprocal lattice vectors involved in spanning the data of Fig. 2.

its arc is 8.66° range, which is noted in Fig. 2(c). This is in excellent agreement with the repeat pattern shown in experiment over ~0°–20°. The shift of the high-symmetry N position lines in experiment and theory from the normal emission direction of $\theta = 0°$ by ~1.6° is simply the effect of the photon wave vector, and is consistent with Fig. 3(b).

We also now consider the impact of slight tilts of the sample surface normal away from the [110] direction, and these are indicated for one-step calculations with two sample orientations: the ideal geometry shown in Fig. 1, and with the [110] direction tilted away from the azimuthal rotation axis toward [101] by 2° in Fig. 4. Significant differences are found over the full angle range of 45° calculated. The best agreement between one-step calculations and experimental data has in fact been found for a tilt angle of 1° toward the [101] direction. It is thus clear that sample orientation must be more precisely controlled in higher-energy ARPES, as expected from the greater magnitude of $\vec{k}_f$.
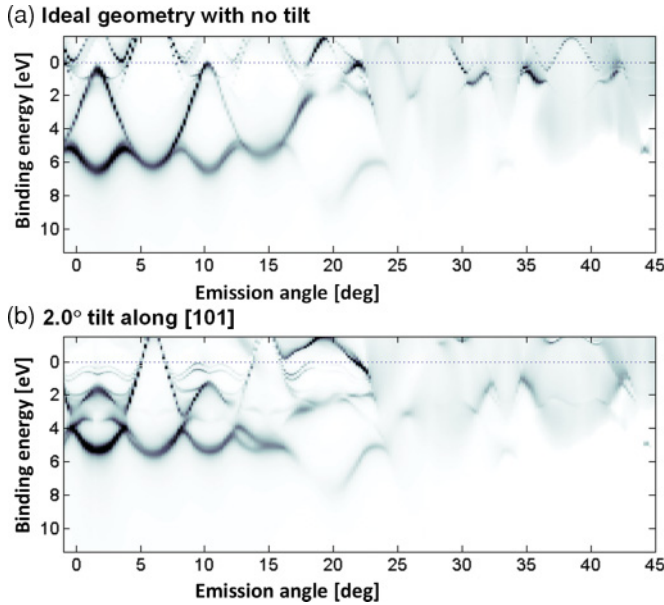
FIG. 4. (Color online) Indication of the sensitivity of soft-x-ray ARPES data to a tilt misalignment of the sample orientation in which the [110] direction is tilted away from the azimuthal axis and towards [101] by 2.0°, as judged by one-step calculations including matrix element effects.

Finally, we consider more generally the range over which reasonable ARPES measurements should be possible as photon energy is increased. As an approximate way to assess the degree of phonon-induced BZ averaging for various systems, we show in Fig. 5(a) the photon energies yielding Debye-Waller factors of 0.5 at 20 K (a reasonable measuring temperature for many current cryocooled sample holders) as a function of atomic mass and Debye temperature, with points for several elements indicated. Other elements or compounds can be estimated from this plot. From this consideration of approximately 40 elements, we conclude that fruitful ARPES measurements should certainly be possible for many materials in the 1–3 keV range. For other materials, and/or with correction procedures such as those indicated in Eqs. (2)–(5), or better methods allowing more precisely for phonon effects, even higher energies up to 6 keV should be possible, with some first data at the latter energy having been obtained for W recently.[34] An additional consideration in such hard x-ray ARPES (HARPES) measurements is the effects of recoil on energy positions and resolutions. Figure 5(b) estimates this in the limit of free-atom recoil, for which the recoil energy can be estimated from Refs. 12,13: $E_{\mathrm{recoil}} \approx \frac{\hbar^2 k_f^2}{2M} \approx 5.5 \times 10^{-4} [\frac{E_{\mathrm{kin}}(\mathrm{eV})}{M(\mathrm{amu})}]$, where M is the effective mass of the atom(s) involved. Here again, with typical resolutions of ~100 meV that can already be achieved with soft and hard x-ray ARPES systems, we find that most elements should be capable of study up to 4 keV, if not higher.

IV. CONCLUSIONS

In conclusion, we have presented $\vec{k}$-resolved high-energy angle-resolved photoemission data for the model system
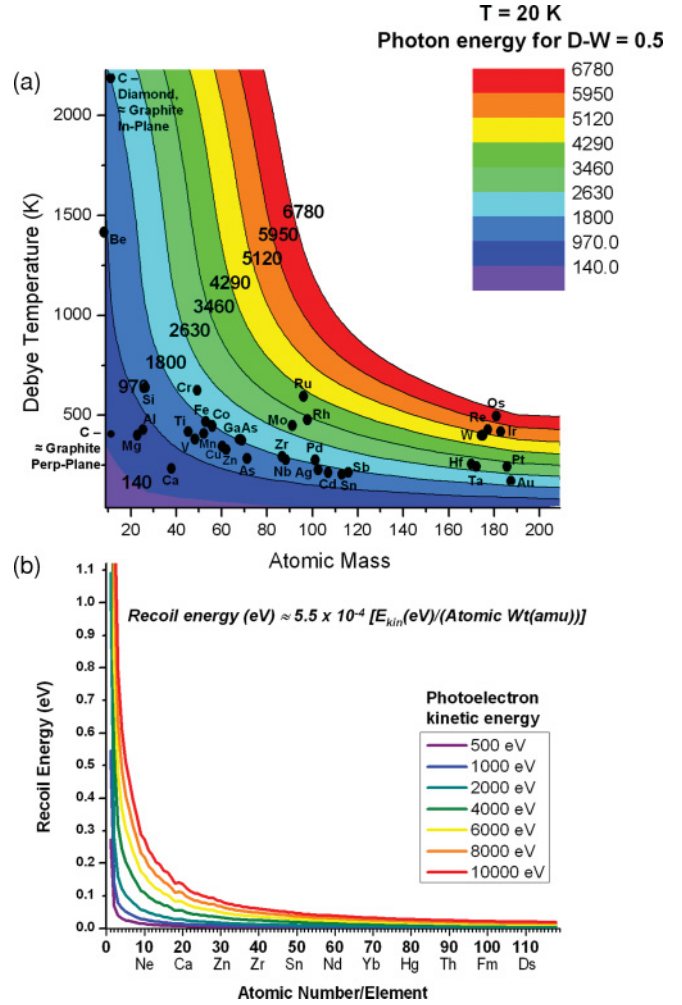

FIG. 5. (Color online) (a) Plot of the photon energies yielding valence-band Debye-Waller factors of 0.5, as a rough estimate of 50% direct-transition behavior, at a 20 K measurement temperature, as a function of atomic mass and Debye temperature. The points show various elements. This plot can be used to estimate the feasibility of high-energy ARPES experiments for other materials. (b) Plot of recoil energy as a function of atomic number and photon energy, permitting an upper-limit estimate of energy shifts and broadening.

tungsten (110) using nonmonochromatized Mg Kα radiation at 1253.6 eV for excitation. We have shown that the observed E-$\vec{k}$ data can in first approximation be understood within a simple free-electron final-state model, and that at a much more quantitative level one-step theory including matrix elements provides an excellent description of our results, including the relative intensities of most features. The effects that must be taken into account are the high photon momentum, electron-phonon interactions that tend to introduce density-of-states-like background in the data, and the specific pathways in $\vec{k}$ space that are represented by the data. This study thus opens the way to doing more bulk-sensitive ARPES even with standard XPS systems, which can have resolutions in energy of 0.5 eV or less with monochromatization, but it also provides further insight into future synchrotron radiation ARPES experiments at energies from 1 keV upward, for which resolutions of as low as 10 meV should be possible. With

tunable synchrotron radiation, three-dimensional (3D) band mapping via Brillouin zone "tomography" should be possible. For example, for the case of tungsten considered here, varying the photon energy in small steps from 1222 eV to 1130 eV in normal emission would permit moving the detector-image cross section in the BZ from the H-N-H line to the H-Γ-H line, thus spanning the full BZ. As a general conclusion, we also suggest that meaningful ARPES measurements should be possible for any system whose Debye-Waller factor at the measurement temperature is >∼0.5, with this further pointing to the 1–3 keV regime as most useful, but higher energies also possible for many materials, particularly as the theory of phonon effects becomes quantitative, thus permitting more

exact allowances for the presence of density-of-states-like intensity across the Brillouin zone.

*pluto@physics.ucdavis.edu

[1] Y. Baer, M. G. Garnier, D. Purdie, P. Segovia, M. Hengsberger, J. Electron Spectrosc. Relat. Phenom. **114-116**, 257 (2001).

[2] F. J. Himpsel, Adv. Phys. **32**, 1 (1983).

[3] C. J. Powell and A. Jablonski, J. Phys. Chem. Ref. Data **28**, 19 (1999).

[4] J. Feydt, A. Elbe, H. Engelhard, G. Meister, C. Jung, and A. Goldmann, Phys. Rev. B **58**, 14007 (1998).

[5] A. Yamasaki, A. Sekiyama, S. Imada, M. Tsunekawa, A. Higashiya, A. Shigemoto, and S. Suga, Nucl. Instrum. Methods Phys. Res. Sect. A **547**, 136 (2005).

[6] M. Yano, A. Sekiyama, H. Fujiwara, T. Saita, S. Imada, T. Muro, Y. Onuki, and S. Suga, Phys. Rev. Lett. **98**, 036405 (2007).

[7] L. Duò, Surf. Sci. Rep. **32**, 235 (1998).

[8] A. Sekiyama, T. Iwasaki, K. Matsuda, Y. Saitoh, Y. Onuki, and S. Suga, Nature **403**, 396 (2000).

[9] T. Iwasaki, A. Sekiyama, A. Yamasaki, M. Okazaki, K. Kadono, H. Utsunomiya, S. Imada, Y. Saitoh, T. Muro, T. Matsushita, H. Harima, S. Yoshii, M. Kasaya, A. Ochiai, T. Oguchi, K. Katoh, Y. Niide, K. Takegahara, and S. Suga, Phys. Rev. B **65**, 195109 (2002).

[10] C. S. Fadley, Nucl. Instrum. Methods Phys. Res. Sect. A **547**, 24 (2005).

[11] T. Claesson, M. Månsson, C. Dallera, F. Venturini, C. De Nadaï, N. B. Brookes, and O. Tjernberg, Phys. Rev. Lett. **93**, 136402 (2004).

[12] S. Suga and A. Sekiyama, Eur. Phys. J. Special Topics **169**, 227 (2009).

[13] S. Suga, Appl. Phys. A **92**, 479 (2008).

[14] Z. Hussain, C. S. Fadley, S. Kono, and L. F. Wagner, Phys. Rev. B **22**, 3750 (1980).

[15] Z. Hussain, E. Umbach, J. J. Barton, J. G. Tobin, and D. A. Shirley, Phys. Rev. B **25**, 672 (1982).

[16] L. Plucinski, J. Minar, B. C. Sell, J. Braun, H. Ebert, C. M. Schneider, and C. S. Fadley, Phys. Rev. B **78**, 035108 (2008).

[17] F. Venturini, J. Minar, J. Braun, H. Ebert, and N. B. Brookes, Phys. Rev. B **77**, 045126 (2008).

[18] W. E. Pickett, Phys. Rev. B **25**, 745 (1982).

[19] G. D. Gaspari and B. L. Gyorffy, Phys. Rev. Lett. **28**, 801 (1972).

[20] C. Søndergaard, P. Hofmann, C. Schultz, M. S. Moreno, J. E. Gayone, M. A. Vicente Alvarez, G. Zampieri, S. Lizzit, and A. Baraldi, Phys. Rev. B **63**, 233102 (2001).

[21] M. A. V. Alvarez, H. Ascolani, and G. Zampieri, Phys. Rev. B **54**, 14703 (1996).

[22] S. Suga, A. Shigemoto, A. Sekiyama, S. Imada, A. Yamasaki, A. Irizawa, S. Kasai, Y. Saitoh, T. Muro, N. Tomita, K. Nasu, H. Eisaki, and Y. Ueda, Phys. Rev. B **70**, 155106 (2004).

[23] A. Sekiyama, S. Kasai, M. Tsunekawa, Y. Ishida, M. Sing, A. Irizawa, A. Yamasaki, S. Imada, T. Muro, Y. Saitoh, Y. ÅŒnuki, T. Kimura, Y. Tokura, and S. Suga, Phys. Rev. B **70**, 060506 (2004).

[24] N. Kamakura, Y. Takata, T. Tokushima, Y. Harada, A. Chainani, K. Kobayashi, and S. Shin, Phys. Rev. B **74**, 045127 (2006).

[25] B. Feuerbacher and N. E. Christensen, Phys. Rev. B **10**, 2373 (1974).

[26] R. C. White, C. S. Fadley, M. Sagurton, and Z. Hussain, Phys. Rev. B **34**, 5226 (1986).

[27] N. E. Christensen and B. Feuerbacher, Phys. Rev. B **10**, 2349 (1974).

[28] V. P. Zhukov and V. A. Gubanov, Solid State Commun. **56**, 51 (1985).

[29] J. Braun, Rep. Prog. Phys. **59**, 1267 (1996).

[30] C. S. Fadley, M. A. Van Hove, Z. Hussain, and A. P. Kaduwela, J. Electron Spectrosc. Relat. Phenom. **75**, 273 (1995).

[31] P. Blaha, K. Schwarz, G. H. K. Madsen, D. Kvasnicka, and J. Luitz, in *An Augmented Plane Wave Plus Local Orbitals Program for Calculating Crystal Properties in WIEN2K*, edited by K. Schwarz (Technische Universität Wien, Vienna, 2000).

[32] A. Bostwick and E. Rotenberg (personal communication).

[33] H. Ebert, in *Lecture Notes in Physics*, edited by H. Dreysse (Springer, Berlin, 2000), Vol. 535, p. 191.

[34] S. Ueda, K. Kobayashi, C. Papp, A. X. Gray, L. Plucinski, J. Minar, J. Braun, H. Ebert, and C. S. Fadley, unpublished results from SPring8 beamline BL15XU.